wave radiometers, and multispectral low-light-level television are presently being installed on aircraft for low-altitude flight. Sensor systems that could detect a surface oil sheen of 1000 m² or greater from high-altitude aircraft with corresponding increased swath width could decrease yearly costs from $11 to $18 million.

Monitoring of Endangered Marine Life

The Marine Mammal Act of 1972 (Public Law 92–522) focused on the need to assess the stock of specific species of marine life to insure their continued existence and on the ultimate goal or restoring and maintaining a viable commerce with certain of these species. The prime current need is to conduct a census of many of these mammals, including, for example, sea otters, and gray and bowhead whales, walrus, and seals. Three specific forms of space technology appear appropriate for development.

1. Tracking of animals by surface, aircraft, or spacecraft techniques, potentially using radar transponders, to determine the habits of the creature; in particular, the time in and out of the water.

2. Overflights by aircraft to determine the herd sizes and numbers of animals in the herds.

3. Where appropriate, satellite tracking of icefields to assess and forecast the location of ice where these animals are most likely to be found, thus reducing aircraft search time.

Benefits are difficult to establish beyond the preservation and conservation of these marine animals.

PART B

TECHNICAL BACKGROUND

N76 11818

SUMMARY

This section describes the physics of electromagnetic scattering from the sea and is presented as a guideline to relate an observable (such as the radar cross section) to the hydrodynamics or physical properties of the sea.

At microwave frequencies, the ocean produces two types of scattering processes. The larger ocean waves essentially behave as an ensemble of specular reflectors such that the strength of the scatter is proportional to the tilts (or slopes) of the gravity waves. Because the length of the ocean wave is much greater than the height, quasi-specular scattering occurs only at angles close to the nadir direction (usually within 25°). Therefore, near nadir, the active microwave system is closely linked with the physics that controls the gravity wave slope. For angles beyond 20°, resonant (Bragg) scattering occurs from those waves that are comparable to the wavelength of the incident electromagnetic wave. At microwave frequencies, this type of scattering is controlled by the capillary wave structure. Because the capillaries have a short time constant for growth and decay, the scattering strength is linked to the local wind fields and the surface tension of the ocean surface.

As specific examples of the interdisciplinary science of electromagnetics and geophysical oceanography, the physics is discussed in connection with data provided by three instruments; namely, the scatterometer, the altimeter, and the imaging radar. These instruments are selected because of the availability of generally consistent data resulting from numerous experiments conducted from stationary platforms, aircraft, and satellites. The data provided by each instrument are discussed in context with

specular point and Bragg scattering theories.

Although the scope of the Active Microwave Working Group is active systems, the physics of the microwave radiometer is discussed as a complementary instrument. Finally, the degrading effect of extraneous sources of noise is discussed as a limiting mechanism of the accuracy of the ocean surface measurement.

PHYSICAL MECHANISMS OF THE RADAR ECHO

Radar echo from the sea was first observed during World War II on shore- and ship-based surveillance systems. Because this echo represented an unwanted signal that often masked the desired target signals, it was referred to as "clutter." Early systems used straightforward techniques to suppress the echoes from these nearly stationary sea scatterers to enhance the returns from faster moving targets. However, little attention was devoted to the actual nature of the sea echo and the scatter mechanisms until the late 1950's.

The first definitive studies on this subject were experimental. Crombie (ref. 3–3) deduced from measured sea echo Doppler spectra that the dominant scatter mechanism at high frequency (hf) (approximately 30 m wavelength) is resonant (or Bragg) scatter, which originates from ocean wavetrains for which the spatial period is one-half the radar wavelength (for backscatter near grazing), and which is traveling toward and away from the radar. Measurements of microwave sea return (approximately 3-cm wavelength), although not immediately identifying the applicable scatter mechanism, showed definite regions and trends in the echo that were functions of frequency, sea state (wind-speed), polarization, and incident angle. Reviews of these early investigations can be found in references 3–4 to 3–6.

Theoretical efforts (refs. 3–7 and 3–8) on the subject of rough surface scattering have also contributed significantly to the interpretation of the physical mechanisms responsible for sea scatter. In particular, the two-scale scattering model (refs. 3–7 and 3–9) has offered satisfactory explanations for most of the observed characteristics of the sea return.

For returns near normal incidence (incident angles less than approximately 20°), theoretical results indicate that the large gravity waves (which are at least several radar wavelengths across) are the dominant contributors to sea return. These gravity waves act as quasi-specular reflectors to which physical optics theory is applicable. The problem may be approached either by computing the surface autocorrelation function (ref. 3–10) needed in the physical optics formulation for a randomly rough surface using the sea spectrum obtained by oceanographers, or by modeling the sea surface by a collection of plane facets (ref. 3–11) and using the measured sea slope distribution for the facets. Such theories have given correct predictions for both the angular and the wind dependence in this region. They also indicate that wind dependence is related directly to the changes in the slope of the density function of the sea surface (ref. 3–12).

For returns away from the normal (incident angles larger than 20°), the dominant contributor to sea return in the microwave region is the capillary wave to which the standard small perturbation theory is applicable (ref. 3–13). The first-order perturbation result shows that the Bragg resonance alone cannot explain the difference in wind dependence between the horizontally and vertically polarized returns (ref. 3–14). The two-scale scattering theory indicates that the interaction between the gravity and the capillary waves must be considered. Such an interaction leads to a stronger wind dependence for the horizontally polarized return, which is exactly what has been observed experimentally (ref. 3–14). The two-scale scattering theory also shows that wind dependence in this angular region is due primarily to the growth of the sea spectrum with the wind, a fact reported by many oceanographers (ref. 3–15).

Before attempting to design a radar experiment for remotely sensing sea state from space, a thorough understanding of the mechanisms responsible for the scattering process should be achieved. Having the mechanisms and the quantitative models that they produce, one can then sensibly analyze a proposed experiment concerning its feasibility, sensitivity, and cost.

The physical mechanisms presently known and accepted as responsible for scatter from the sea are summarized in table 3–II. Bragg scatter is illustrated in the experimental record at 10 MHz shown in figure 3–1. The two dominant "spikes" in the Doppler spectrum occur at shifts of $\pm [g/(\pi\lambda)]^{1/2}$, where g is the acceleration of gravity and λ is the radar wavelength. This is confirmed by derivations from the first-order theory, which is summarized as

$$\sigma_{VV}(\eta) = 2^5 \pi k_0^4 \ [\sin \theta_i \sin \theta_s + \cos(\phi_i - \phi_s)]^2$$

$$[S_{\pm}(\kappa_{rx}, \kappa_{ry})\delta(\eta \pm \omega_g)] \qquad (3\text{--}1)$$

where

$\sigma_{VV}(\eta)$ = normalized Doppler spectrum backscattering cross section for vertical-transmit, vertical-receive polarization states
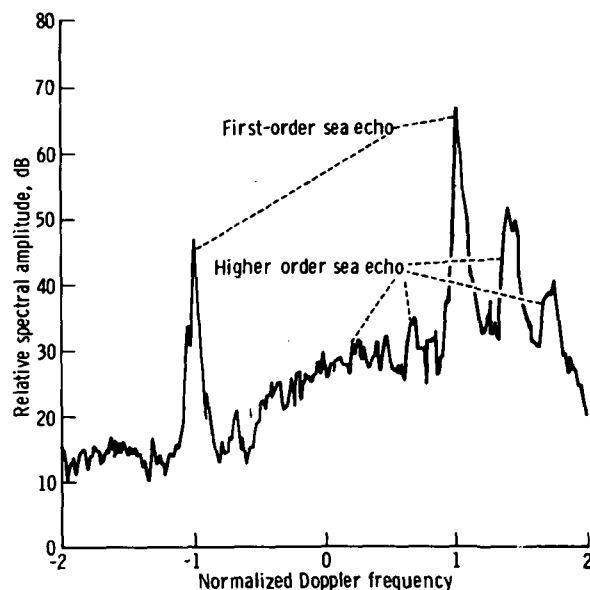

FIGURE 3–1.—Illustration of Bragg scatter at 10 MHz.

η = radian Doppler shift from carrier $= \omega - \omega_0$

ω = temporal wave number of ocean wave

ω_0 = radian wave number of radio carrier frequency

κ_r = sum of incident and scattered radar wave numbers $= \mathbf{k}_i + \mathbf{k}_s$

$\mathbf{k}_i = k_0 (\sin \theta_i \cos \phi_i \ \mathbf{x} + \sin \theta_i \sin \phi_i \ \mathbf{y} - \cos \theta_i \ \mathbf{z})$

$\mathbf{k}_s = k_0 (\sin \theta_s \cos \phi_s \ \mathbf{x} + \sin \theta_s \sin \phi_s \ \mathbf{y} + \cos \theta_s \ \mathbf{z})$

k_0 = radar wave number $= 2\pi/\lambda$

ω_g = Doppler shift of advancing and receding resonant gravity waves $= g^{1/2} (\kappa_{rx}^2 + \kappa_{ry}^2)^{1/4}$

$S_{\pm}(\kappa_{rx}, \kappa_{ry})$ = directional wave-height spectrum of ocean waves, where the $\pm$ subscript refers to spectra representing waves advancing and receding along κ_r (x, y)

(θ, ϕ) = polar angles associated with transmitted and received wave directions

s, i = subscripts indicating scattered and incident, respectively

$\mathbf{x}, \mathbf{y}, \mathbf{z}$ = unit vectors along the x-, y-, and z-axis, respectively

λ = radar wavelength

δ = Dirac impulse function

In equation (3–1), the Doppler spectrum is shown to consist of two impulse functions (or spikes) in the frequency domain centered at shifts $\pm [(2k_0 g)/(2\pi)]^{1/2} = [g/(\pi\lambda)]^{1/2}$ for backscatter near grazing $(\phi_s = \phi_i, \ \theta_s = \theta_i =$

TABLE 3–II.—*Physical Mechanisms of Radar Scatter From the Sea*

Scatter	Physical mechanisms
mf/hf (1000 m$>\lambda>$10 m)[a]	Bragg (diffraction grating) effect.
Microwave (1 m$>\lambda>$1 mm)	Quasi-specular reflections (diffraction) (within 15° of specular direction). Bragg (diffraction grating) effect and interaction between large- and small-scale waves (beyond 15° of specular direction).

[a] Medium frequency/high frequency; $\lambda =$ wavelength.

$\pi/2$). Furthermore, the magnitude of the echo as contained in these spikes is proportional to the wave-height directional spectrum evaluated at twice the radar wave number ($2k_0$). Bragg scatter in other directions follows analogously. The ocean wave train that scatters in a given direction (θ_s, ϕ_s) has a spatial period $L=2\pi/|\kappa_r|$ and orientation given by $\phi_r=\tan^{-1}(\kappa_{ry}/\kappa_{rx})$ with respect to the x-axis.

At microwave frequencies, the average radar backscattering cross section as a function of angle of incidence typically has the shape shown in figure 3–2. The scattered echo signal in the region with 15° to 25° from the vertical is referred to as the quasi-specular component and can be explained by reflections from plane facets. In the high-frequency limit, the average backscatter cross section per unit surface area for this component is given as

$$\sigma^\circ = \pi \sec^4 \theta \, P(\zeta_{xsp}, \zeta_{ysp}) \, |R(0)|^2 \quad (3\text{–}2)$$

where

σ° = average backscatter cross section per unit area for polarized component
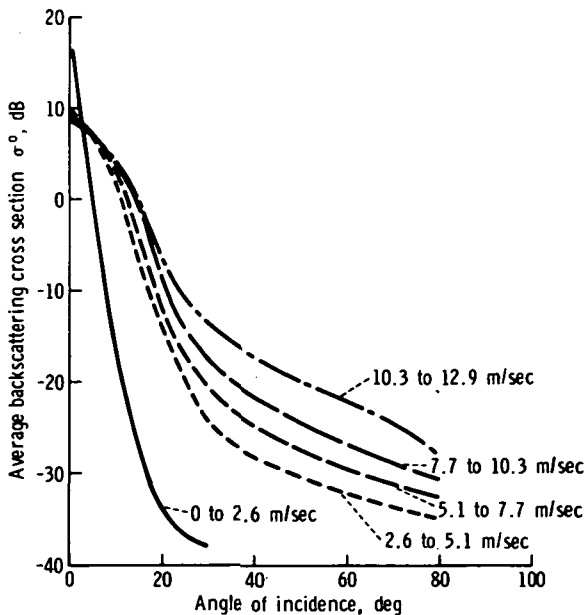

FIGURE 3–2.—Typical average backscattering cross section as a function of incident angle (1.25 cm).

$P(\zeta_x, \zeta_y)$ = probability density function of surface slopes ζ in x and y directions

$\zeta^2_{xsp}+\zeta_{ysp}$ = required specular (mirror) reflection condition at surface facet=$\tan^2 \theta$

$R(0)$ = Fresnel reflection coefficient of sea at normal incidence

θ = angle of incidence (angle between local normal at the surface of scattering and the incident wave direction)

For the sea, the probability density function for the surface slopes is nearly Gaussian. The nature of the continuous sea surface (except under extreme conditions of breaking waves) is such that the slope rarely exceeds 15° to 25°; hence, specular point return would become very weak for incident angles beyond approximately 25°. Because the slope itself is a function of sea state and windspeed, this limit will vary somewhat: between approximately 8° and 15° for the sea states between about sea state 1 (2.5-m/sec wind) and sea state 6 (16-m/sec wind).

One further effect is worth noting in this quasi-specular region: both theory and experiment show that the return is not polarization sensitive. As long as the "polarized" component of backscatter is being received (e.g., vertical received for vertical incident, horizontal received for horizontal incident, left-circular received for right-circular incident, etc.), the magnitude as a function of incident angle is the same; no depolarization is predicted in the near-vertical angular region. This is not true as one moves away from the quasi-specular region, where the vertically polarized backscatter return is usually much larger than the horizontally polarized return in the Bragg scatter region.

Beyond incident angles of approximately 15° to 25°, microwave sea backscatter can be explained to a large extent by the Bragg diffraction grating mechanism. Although the theory appears strictly justifiable only when the overall height of the surface is small in terms of the radar wavelength (which is never true for the sea in the microwave re-

gion), an argument can be made that the sea is really a two-scale composite surface, in which a small-scale slightly rough component is riding on top of much larger waves. According to this composite theory (refs. 3–7, 3–9, 3–16, and 3–17), it is mainly the small-scale component that the radar is observing at these large angles. Although the mathematical justification of the theory can be questioned, extensive experimental work by Guinard and Daley (ref. 3–18), Moore et al. (ref. 3–14), Bradley (ref. 3–19), and Wright (ref. 3–7) indicates that this explanation and theory are reasonably accurate. The magnitude of the radar return as a function of incident angle, the polarization dependence, the frequency dependence, and the Doppler characteristics are all predictable from this two-scale surface model.

Experiments to determine the radar response of the sea have been carried out by numerous investigators. The empirical observation that radar cross section increased with increasing sea state was evident from the start. Some of the conclusions reached by the many investigators have been confusing, however, because of the variety of incident angles used and because of difficulties in obtaining adequate measurements of the sea and wind to compare with the radar observations.

The recent programs (since about 1966) conducted by the Naval Research Laboratory (NRL) and NASA Lyndon B. Johnson Space Center (JSC) have led to a fuller understanding of both the wind response of the capillary waves and the corresponding increase in microwave backscatter.

Claassen et al. (ref. 3–20) reported information on the increase in capillary wave spectral components with windspeed as shown in figure 3–3 (ref. 3–21), where $D(U_*)^{1/2}$ is a wind-dependent coefficient of the capillary part of the wave spectrum. Because the previously described theories indicate that the radar signal should increase as the capillary wave components of the sea increase, the result reported by these authors is most encouraging.
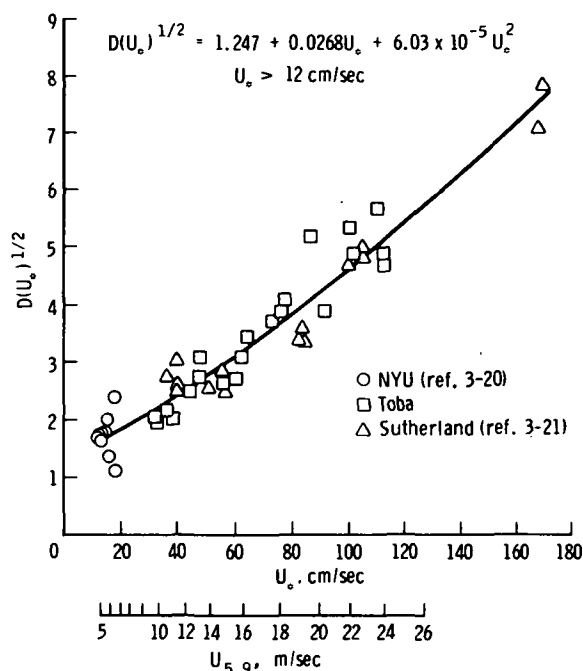

FIGURE 3–3.—The wind dependence of $D(U_*)^{1/2}$ for capillary waves, where U_* is the friction velocity at the ocean surface, and $U_{5.9}$ is the wind velocity at an elevation of 5.9 m above the ocean surface (refs. 3–20 and 3–21).

The JSC and NRL measurements are summarized in reference 3–14. In both cases, measurements made in different years were separated from each other by biases, but individually they exhibited approximately the same wind response. Figures 3–4 and 3–5 show examples of the two data sets plotted on logarithmic scales (the linear decibel scale is a logarithmic amplitude scale). The slope of the trend lines on these curves is the exponent of the wind response for the angle, frequency, polarization, and direction. These responses were found to vary between linear and square law; that is, the exponents were between 1 and 2. Figure 3–6 shows the upwind vertical polarization case.

The variation of response with angle between wind direction and look direction for the radar was somewhat uncertain until the Advanced Application Flight Experiments (AAFE) radiometer/scatterometer (RADSCAT) instrument was flown. This instru-
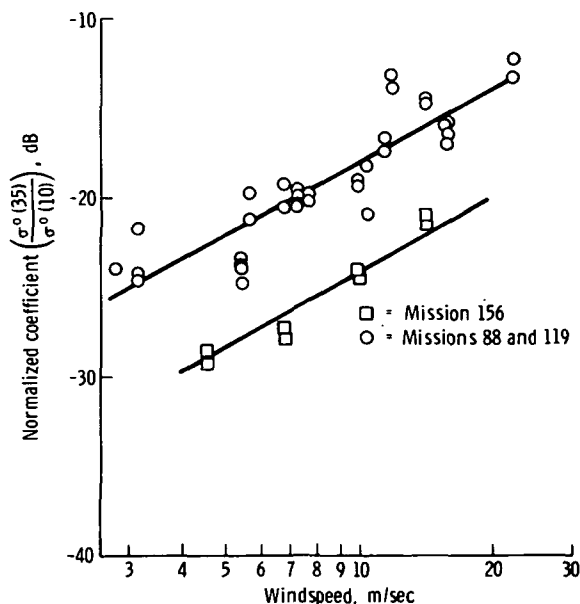
FIGURE 3–4.—Wind response of JSC scatterometric data for crosswind observations (vertical transmit/vertical receive polarization).

ment gave a much clearer identification of the angular variation that must be considered in using backscatter data for wind determination than had previously been available.

Skylab S193 results, although presently incomplete, tend to confirm the previous experiments and to reduce the variance associated with the aircraft experiments. Figure 3–7 shows some of the early results for horizontal polarization (after aspect angle correction).

THE PHYSICS OF THERMAL EMISSION IN THE MICROWAVE BAND

Thermodynamics of Radiometric Emission

The basic physics of thermal emission, regardless of the electromagnetic wavelength, is based on the Planck radiation law. In the microwave region, the Rayleigh-Jeans limit is applicable, and the received power is given by

$$\frac{P_r}{k\Delta f} = T_A = \frac{\int f(\Omega)\, T_B(\Omega)\, d\Omega}{\int f(\Omega)\, d\Omega} \qquad (3\text{--}3)$$
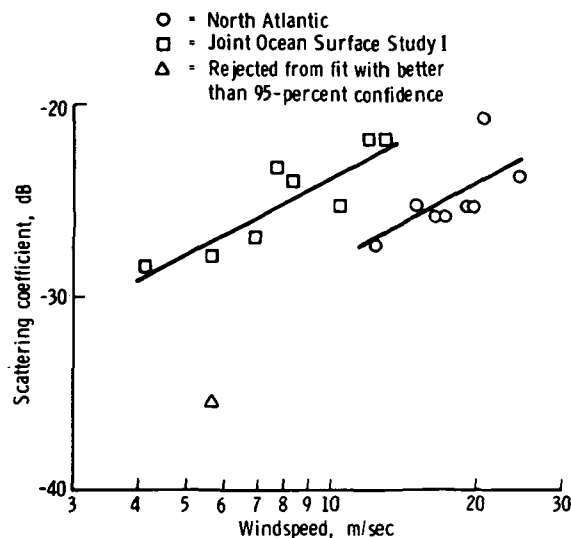

FIGURE 3–5.—Wind response of NRL X-band data for upwind observations at an incident angle of 60° (vertical transmit/vertical receive polarization).

where

$P_r =$ received power

$k =$ Boltzmann constant

$\Delta f =$ receiver bandwidth

$T_A =$ antenna temperature

$f(\Omega) =$ normalized pattern function of the receiving antenna

$T_B(\Omega) =$ brightness temperature
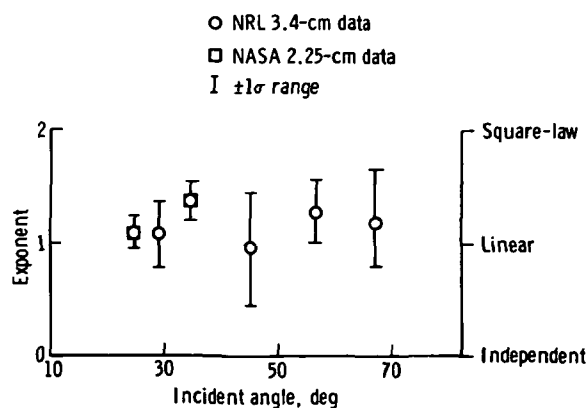
$\Omega =$ solid angle

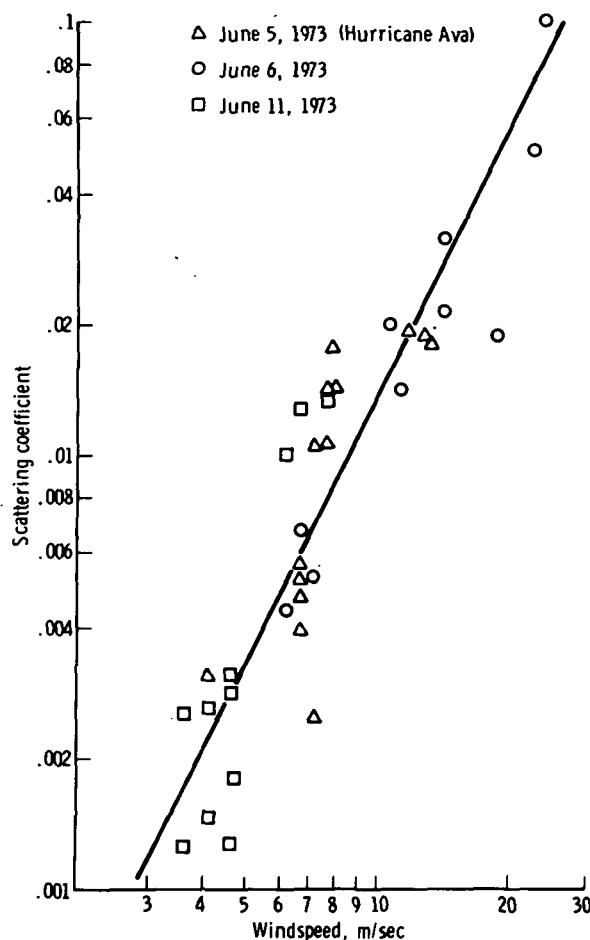FIGURE 3–6.—Wind response of scatterometer (upwind, vertical transmit/vertical receive polarization).

FIGURE 3–7.—The S193 scatterometer response to wind at sea, 30 days into the first Skylab mission (horizontal polarization; 50° angle with vertical).

If atmospheric contributions are ignored, the quantity $T_B(\Omega)$ is the product of the surface emissivity and the molecular temperature of the source.

Emission From a Specular Surface

If the surface is flat, the emissivity E is

$$E = 1 - |R|^2 \qquad (3\text{–}4)$$

where $|R|^2$ is the reflection coefficient, defined by the usual Fresnel expressions. In general, $|R|^2$ is a function of polarization, viewing angle, operating frequency, and dielectric constant. The emissivity of seawater (at the vertical viewing angle) increases from approximate values of 0.3 at 1 GHz to

0.5 at 35 GHz, so that the brightness temperature ranges between 100 and 150 K within the microwave region. As the wavelength decreases to the millimeter range, the emissivity gradually increases to unity.

In addition to radiation being emitted by the surface, sky noise is reflected from the surface into the instrument. This noise is generated by molecular species (principally oxygen and water vapor) and condensed water (clouds and rain) and requires a correction to the radiative transfer order to properly interpret the surface characteristics. The correction is made by using the standard radioactive transfer equations. The atmospheric radiation depends strongly on electromagnetic frequency, relative humidity, and rainfall rate. As a numerical example, the sky temperature increases from approximately 5 K at 1 GHz to approximately 100 K at 22 GHz.

If the surface is indeed flat, or specular, the radiometric emission is a function of only two parameters; namely, the salinity and the temperature of the water. If the water is covered by a layer such as ice, oil, or foam, the reflection coefficient will vary according to the thickness of the layer. If the losses of the layer are not too appreciable, the reflection coefficient will alternately exhibit maximums and minimums at quarter wavelength (layer thickness) intervals. An example of this behavior is shown in figure 3–8, which typifies the way the reflection coefficient
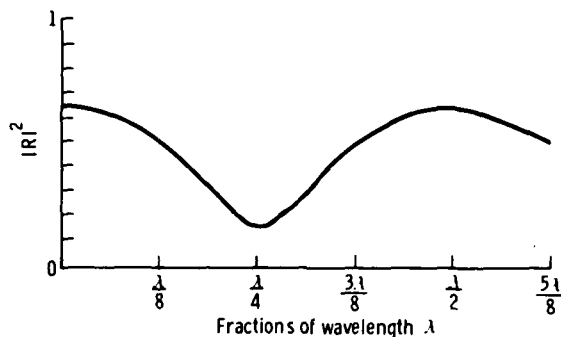

FIGURE 3–8.—Variation in reflection coefficient as a function of thickness in fractions of wavelengths within an ice layer (normal incident angle).

varies as a perfectly smooth ice layer thickens over freshwater. This curve clearly indicates that (1) it is possible to measure the *thickness of smooth layers over the surface* of the water and (2) as the dielectric constant of the layered medium approaches a matched condition, with $|R|^2 \rightarrow 0$ at odd quarter-wavelength intervals, the change in thickness can radically alter the radar cross section.

Relationship Between Microwave Emission, Sea State, and Winds

The determination of sea-state and surface wind fields over the oceans by remote passive microwave sensing has generated much interest during the last decade. Measurements of this type on a temporal, global, and all-weather basis would be of great value to the meteorologist and oceanographer and would be of general maritime use.

The microwave brightness temperature dependence on sea state (windspeed W) arises from two effects. The first effect is a result of the increasing roughness of the compact water surface, and the second effect is a

result of the increasing coverage of whitecaps and sea foam with increasing windspeed. Although both are properly termed roughness effects, the first will be referred to as the surface roughness and the second as the sea-foam effect. Surface roughness has been investigated theoretically using a geometric optics model (ref. 3–22) based on the sea-surface slope distribution of Cox and Munk (ref. 3–23) and using a physical optics model (refs. 3–16 and 3–24) that depends on the correlation function heights.

Multiple-scatter and shadowing effects, which become important at large angles of incidence, have been investigated using a one-dimensional geometric optics model (ref. 3–25). These investigators have shown that the emission from a rough surface is intimately related to the radar scattering coefficient and is explicitly given by

$$E = 1 - \frac{1}{4\pi \cos \theta} \iint \sigma^\circ (\Omega) \, d\Omega \qquad (3\text{–}5)$$

where θ is the incident angle. The quantity σ° also replaces the reflection coefficient to account for the scattered sky component. If σ° is computed from the geometric optics expression, results typical of those shown in figure 3–9 are obtained. These curves show
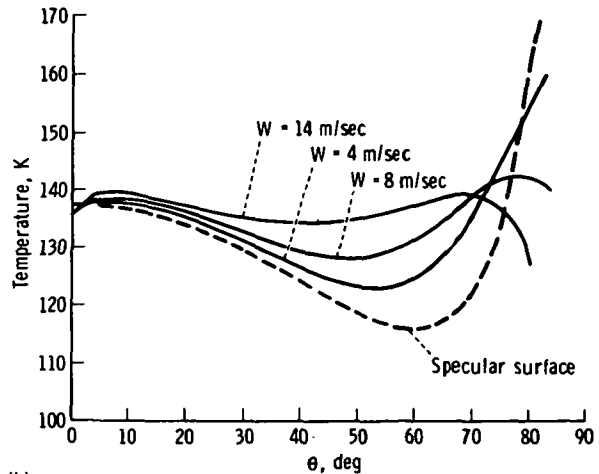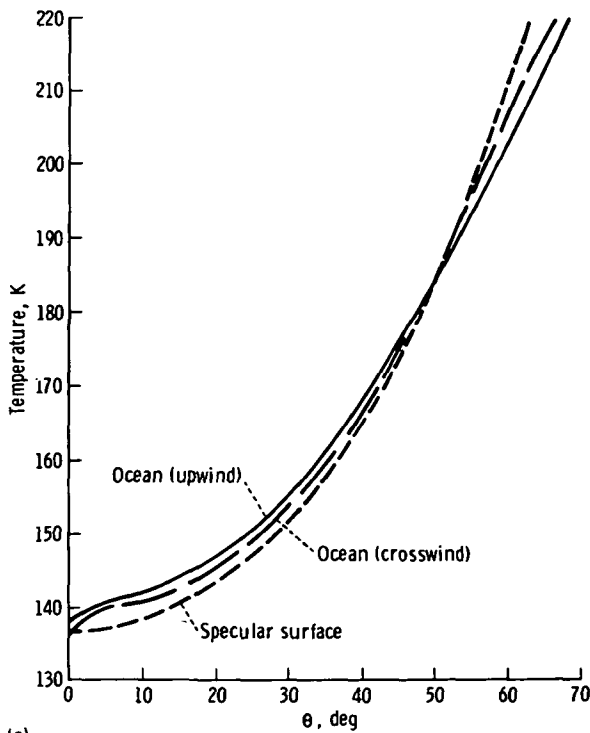
(a)

(b)

FIGURE 3–9.—Brightness temperature as a function of incident angle with wind-roughened ocean surface as a parameter (frequency of 19.4 GHz, water temperature of 290 K). (*a*) Vertical polarization (windspeed of 14 m/sec). (*b*) Horizontal polarization.

that, for the vertical polarization, there is a crossover point; that is, roughness causes an increase in brightness temperature for angles near nadir and a decrease in brightness temperature as the incident angle approaches grazing. Hence, the radiometric temperature is invariant with roughness at the crossover point. For the horizontal polarization, roughness generally causes an increase in brightness temperature over all incident angles. The rather complicated behavior of the family of curves beyond an incident angle of 60° is due to scattered atmospheric radiation, which can be a predominant factor near grazing.

The very high microwave brightness temperature of sea foam compared to that of the average sea surface, which results in the sea-foam effect, was first suggested by Williams (ref. 3–26) and has been supported theoretically on the basis of a physical model for foam (ref. 3–27). Measurements of the microwave brightness temperature of sea surface indicate a dependence on surface roughness and sea foam that is correlated with windspeed (refs. 3–28 to 3–31).

Surface roughness effects will dominate at the lower windspeeds. However, because of the increasing prevalence of sea foam with increasing sea state and the high microwave brightness temperature of foam, the microwave emission characteristics of the sea will be determined by sea foam at very high speeds. The transition windspeed between the two effects is not known but is probably between 15 and 20 m/sec. An estimate of the combined effect of surface roughness and sea foam with windspeed, as viewed from a satellite, is shown in figure 3–10 (ref. 3–32). The effect of surface roughness is seen to predominate at windspeeds to approximately 20 m/sec, with foam being the major factor at higher windspeeds. The combined effects result in a strong windspeed dependence that allows remote sensing of surface wind fields over the entire range of windspeeds from calm to 30 m/sec and higher.

To cover the entire range of windspeeds, observations will be necessary at larger in-
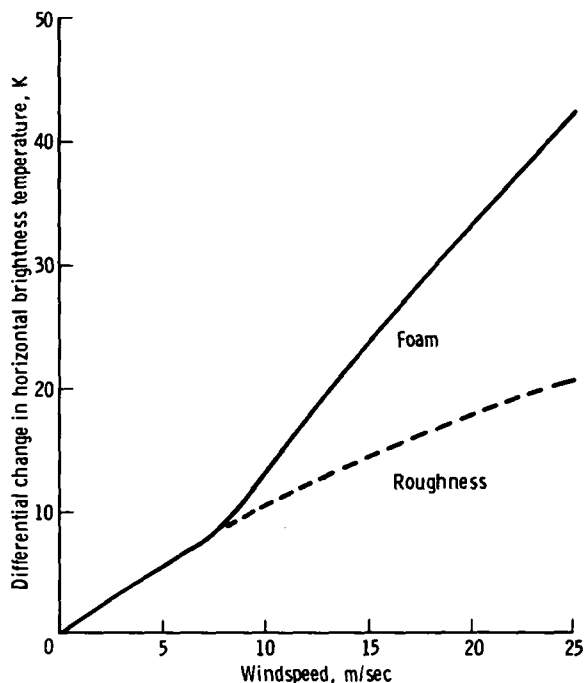

FIGURE 3–10.—Total windspeed dependence at 55° incident angle. The estimated total differential change in horizontal brightness temperature at 19.34 GHz and 55° incident angle is shown as a function of windspeed by the upper solid line. The relative contributions due to surface roughness and sea foam are indicated.

cident angles because the roughness effect is less at the smaller angles. Because the surface roughness effect decreases with decreasing frequency and the foam effect is also likely to decrease, the sensitivity to surface windspeed is greater at higher frequencies. The relative effects of surface roughness and foam may best be studied by simultaneous measurements of both vertical and horizontal polarization at 55° incident angle. The vertical component is sensitive only to foam, whereas the horizontal component is affected by both foam and roughness.

In summary, the microwave brightness temperature of the ocean is significantly dependent on the surface wind fields. This dependence offers the potential to remotely sense surface winds over the entire range of windspeeds from calm to 30 m/sec and higher from a satellite on an all-weather and global

basis. The dependence results primarily from surface roughness effects for windspeeds as high as approximately 15 to 20 m/sec and is largely due to the effects of ocean foam for higher windspeeds. Sensitivity to windspeed increases with frequency and is most pronounced for horizontal polarization at larger incident angles.

ATMOSPHERIC ATTENUATION AND SKY NOISE

When radar measurements of a desired observable are conducted through a long path length of intervening medium, several undesirable results may occur. First, the medium can remove electromagnetic energy from the beam by attenuation and scattering, which will reduce the amount of power received by the radar and therefore restrict the dynamic range of the instrument, or even eradicate the measurement entirely. Another undesirable aspect is that the index of refraction of the medium will affect the group velocity of the electromagnetic wave, thereby resulting in unwanted dispersion and time delay for altimetry. Finally, the noise temperature of the intervening medium increases with absorption, resulting in a reduction of the signal-to-noise ratio.

The pertinent medium is, of course, the atmosphere. The atmosphere removes power from the beam either through resonant absorption by molecular species or by condensed water vapor. Pulse dispersion occurs because the index of refraction is frequency dependent. Absorption and dispersion are most severe when the radar system is tuned to operate near the resonant lines of the atmosphere at 22 GHz (water vapor) and 60 GHz (oxygen).

Details of the undesirable effects can be inferred from the papers concerning the sensing of atmospheric properties. As a general statement, any physical phenomenon that enhances the atmospheric measurement results in a degradation of the oceanographic measurement. This is particularly true if the experiments are conducted from space.

The strongest source of sky noise is the Sun. The radiometric temperature of the quiet Sun ranges from 10^4 K at X-band to 10^5 K at L-band. The "slowly varying component," which is due to sunspot activity, raises these numbers by one to two orders of magnitude, and bursts will raise the temperatures to 10^9 to 10^{10} K. If a radar or radiometer is pointing at an area of the ocean where a strong specular component of the Sun is being reflected from the water, noise may saturate the receiver.

PHYSICAL PROPERTIES OF WATER

The physical properties of water that affect the electromagnetic interaction are the salinity and temperature of the water. These two quantities are important because the complex dielectric constant, and hence the reflectivity, is a function of both salinity and temperature.

Experiments currently indicate that the complex dielectric constant can be cast in the Debye form

$$\epsilon = \epsilon' + i\epsilon'' = \epsilon_\infty + \frac{\epsilon_s - \epsilon_\infty}{1 - i\omega\tau} + i\frac{\rho}{\omega\epsilon_0} \qquad (3-6)$$

where

$\epsilon' =$ dielectric constant
$\epsilon'' =$ loss factor
$\epsilon_\infty =$ the relative dielectric constant as $\omega \to \infty$
$\epsilon_s =$ the relative dielectric constant as $\omega \to 0$
$\omega = 2\pi f$
$\tau =$ relaxation time (sec)
$\epsilon_0 =$ permittivity of free space (8.854×10^{-12} F/m)
$\rho =$ dielectric conductivity
$i = (-1)^{1/2}$

The quantities ϵ_s, τ, and ρ are all functions of temperature and salinity. Stogryn (ref. 3-33) has examined the experimental data and developed analytical expressions for these quantities in terms of regression series. When the dielectric constant is specified, the reflection coefficient $|R(0)|^2$ can be derived from the Fresnel formulas, which, for normal incidence, is given by

$$|R(\theta = 0)|^2 = \left|\frac{1 - \sqrt{\epsilon}}{1 + \sqrt{\epsilon}}\right|^2 \qquad (3-7)$$

It is of interest to note that the geometric optics expression for the radar scattering coefficient of rough surfaces is proportional to $|R(\theta=0)|^2$.

Figure 3–11 shows a plot of reflection coefficient as a function of frequency values that $|R(0)|^2$ may assume because of extreme variations in the water temperature and salinity content (0 to 35‰). At frequencies above 5 GHz, the change in $|R(0)|^2$ is primarily due to the influence of water temperature. As the frequency decreases below 5 GHz, salinity becomes a more important parameter. The gross knowledge of the reflection coefficient is important for the system design. First, the scattered signal is 2 to 3 dB less than what it would be if the ocean were a perfect reflector; second, if $|R(0)|^2$ is less than unity, thermal radiation is emitted that decreases the signal-to-noise ratio of the measurement. The detailed knowledge of the variation of reflection coefficient with salinity and temperature appears to be of minor importance. Because the data in figure 3–11 only span 1.88 dB, the measurement of $\sigma°$ must be done to within a few hundredths of a decibel for active systems to provide accurate temperature ($\Delta T = 10°$) and salinity ($\Delta S = 1‰$) measurements
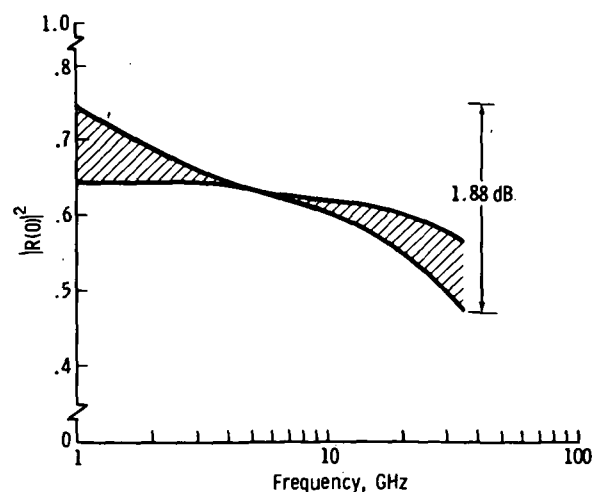
of water. Such measurements can apparently best be done with microwave radiometers. When water turns to ice, the static dielectric constant remains unchanged; however, the relaxation time τ increases by several orders of magnitude. Assuming that the ice is frozen freshwater (i.e., $\rho=0$), then a large $\omega\tau$ in the Debye equation gives a value ϵ of approximately ϵ_x plus a small imaginary part (or $\epsilon\approx4.9$), in which case $|R(0)|^2$ is approximately 0.14. This very low loss, which results from the significant increase in $\omega\tau$, serves to increase the skin depth and enables the radar to illuminate features covered by snow and ice.

APPLICATIONS OF PHYSICS TO RADAR SENSING TECHNIQUES

The purpose of this section is to examine several concepts for instruments that could possibly measure some of the important properties of sea state. In this section, the various instruments will not be compared concerning their sensitivity, performance, and cost; that will be done in a subsequent section of this document. Rather, the physical mechanism of radar scatter in the operation of the instrument will be examined and it will be shown how the theoretical concepts and equations of the section entitled "Physical Mechanisms of the Radar Echo" can be applied to quantitatively explain the performance of the sensors. The principal instruments to be examined in this respect are as follows.

1. Scatterometer: Mean slopes near vertical are sensitive to sea state. Bragg scatter from capillary waves at angles sufficiently removed from nadir is sensitive to the instantaneous windspeed.

2. Altimeter: Distribution of specular points at vertical is proportional to the height distribution of the largest waves.

3. Imaging radars/wave spectrometers: Local tilts of specular points (and hence local echo intensity) vary with the slope of longer waves.

FIGURE 3–11.—Plot of reflection coefficient as a function of frequency over the microwave band of 1 to 35 GHz.

In addition to these well-known sensors, several other concepts that could also have spacecraft application will be described.

Scatterometry

The scatterometer is the simplest form of microwave radar. It senses the (averaged) absolute power return from the sea surface. The instrument parameters that can usually be varied for a particular scatterometer system are the incident angle and the polarization states. Because the instrument is usually well calibrated, it is possible to measure $\sigma°$, the average radar backscatter cross section of the sea surface per unit surface area, as a function of incident angle and polarization state. The scatterometer has already been flight tested aboard numerous aircraft and has been flown on Skylab; specific results are discussed in subsequent sections of this report.

The normal incident angle range of the instrument is from the vertical out to 60°. Near the vertical ($\theta < 20°$), the specular-point theory discussed in the section entitled "Physical Mechanisms of the Radar Echo" is applicable. The radar scatter model is given in equation (3–2). Because the slopes for the sea are usually Gaussian distributed, equation (3–2) can be rewritten

$$\sigma° = \frac{\sec^4 \theta}{2\zeta_x \zeta_y} \exp\left(-\frac{\tan^2 \theta}{2\zeta_x}\right) |R(0)|^2 \qquad (3–8)$$

where ζ_x and ζ_y are the root-mean-square (rms) sea slopes in the x and y directions, with the x-direction here being taken to lie along the surface in the plane of incidence. Again, $R(0)$ is the Fresnel reflection coefficient of a smooth sea at normal incidence. Thus, by measuring $\sigma°$ as a function of θ, one can potentially measure the surface slopes of the sea. Because these slopes are related to sea state and/or windspeed, it should be possible to determine these meteorological parameters with the scatterometer.

An example of one possible straightforward relationship between surface slope and windspeed is shown in figure 3–12 (ref. 3–34), which gives both measured data and a
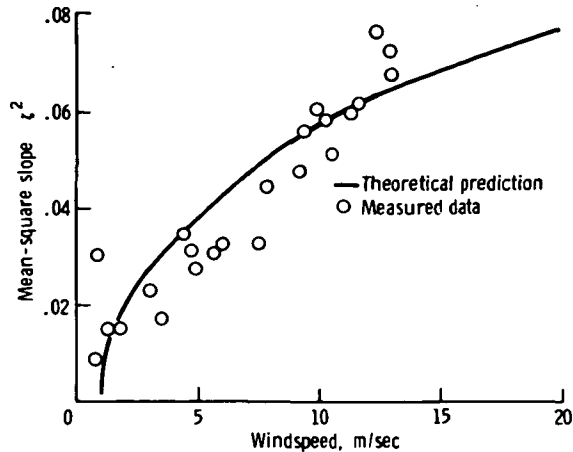

FIGURE 3–12.—Example of possible relationship between sea surface slope and windspeed.

theoretical prediction for the variation of the sea surface slope with windspeed. If the further simplifying assumption is made (though it may not be necessarily valid) that the sea-slope distribution is isotropic, then the expression for $\sigma°$ can be simplified still further. In this case, $\zeta_x^2 = \zeta_y^2 = \zeta^2/2$, where ζ^2 equals $\zeta_x^2 + \zeta_y^2$ and is the total mean-square slope of the surface. Then, at the vertical,

$$\sigma° = \frac{|R(0)|^2}{\zeta^2} \qquad (3–9)$$

The slope-dependent specular-point theory can provide a reasonable basis for the design and interpretation of scatterometer data out to incident angles of approximately 20°.

An important question that has an impact on scatterometer accuracy is the variance around the apparent mean of the measured sea-echo points, which is evident in experimental data. No simple theoretical model completely explains the reason for this variance. It is quite obvious that this variance in sea echo, combined with instrumental and propagation loss variances, will ultimately limit the accuracy of the scatterometer for measuring the surface winds.

The bulk of scatterometer data, which has been obtained by NRL, NASA JSC, and NASA Langley Research Center (LaRC), has concentrated on the response at viewing

angles greater than 25°. The rationale be-
hind the desire to operate in this mode is
twofold: first, the scattering data are pro-
portional to the local wind sector (which is
of interest for meteorological forecasting),
and second, the wide-angle scan will give
wide-area global coverage from satellite plat-
forms. As previously mentioned, Bragg
scattering dominates in this mode of the
scatterometer. Specific descriptions of the
theoretical model and a discussion of flight
results are presented in detail in a subsequent
section. Scatterometers have also been used
in the detection of oil spills (ref. 3-35).

Altimetry

An orbiting microwave altimeter trans-
mits a pulse with an effective spatial length
that is short compared to typical wave
heights (e.g., usually less than 0.5 m). As the
pulse interacts with waves beneath the satel-
lite, it is scattered back toward the satellite
by specular points on the larger gravity
waves. The short pulse is "stretched" tempo-
rarily by the ocean waves, and the degree of
this stretching is a direct measure of the
mean heights of the waves at the suborbital
point. The radar altimeter has been tested on
various aircraft and on Skylab. The pulse
length on Skylab, however, was insufficiently
short to allow a good test of the sensor for
measuring wave height. The primary satel-
lite tests of the instrument are to be con-
ducted with the Geodynamic Experimental
Oceanic Satellite (GEOS–C), which is to be
launched in 1975.

The radar cross section can be expressed
as a function of the height of the radar pulse
interaction region, as shown in equations
(3–10) and (3–11). From the specular-point
theory discussed in the section entitled
"Physical Mechanisms of the Radar Echo,"
backscattered strength from N specular
points is

$$\sqrt{\sigma_B} = \sum_{i=1}^{N} \sqrt{\pi g_i} \, e^{i2k_o Z_i \cos \theta} \qquad (3\text{--}10)$$

where
  $g_i =$ Gaussian curvature at the ith specular
     point
  $Z_i =$ height of the ith specular point above
     mean surface
  $k_o =$ radar wave number
  $\theta =$ angle of incidence from vertical

When equation (3–10) is squared, written as
a distribution over height, and averaged, it
becomes

$$\eta^\circ (Z) = \pi \int_0^\infty n(Z,g) \, g \, dg \qquad (3\text{--}11)$$

where $\eta^\circ (Z)$ is the average backscatter cross
section per unit area per unit height incre-
ment at height Z, and $n(Z, g)$ is the average
number of specular points per unit area for
heights between Z and $Z+dZ$ and for Gaus-
sian curvature between g and $g+dg$.

The physical illustration of a radar pulse
of spatial width $\Delta Z \cos \theta = (c\tau)/2$ advancing
over the ocean is shown in figure 3–13. If
this model is used, and it is assumed that a
symmetric Gaussian distribution of sea-wave
heights exists, the expression in equation
(3–12) is obtained for the average radar
cross section of the sea as a function of time.
Radar altimeter power return $(H \ll a)$ is

$$G^2 \sigma(t) = \sqrt{\pi^3} \, \frac{H x_w}{s^2} \exp \left[\left(\frac{t_p}{t_s} \right)^2 - \frac{2t}{t_s} \right]$$

$$\left[1 - \phi \left(\frac{t_p}{t_s} - \frac{t}{t_p} \right) \right] \qquad (3\text{--}12)$$

where
    $G =$ antenna gain as a function of time
  $\sigma(t) =$ average radar cross section as a
     function of time
    $H =$ height of the radar altimeter
    $a =$ "radio" radius of the Earth ($\approx 4/3$
     times actual Earth radius)
   $s^2 =$ total slope
  $x_w = (c\tau)/[4 (\ln 2)^{1/2}]$
  $t_p = [2 (x_w{}^2 \; 2h^2)^{1/2}]/c$
  $t_s = (2H^2 \Psi_e^2)/c$
  $1/\Psi_e^2 = [(8 \ln 2)/\Psi_B{}^2] + (1/s^2)$, where Ψ_e
     and Ψ_B are shown in figure 3–14
   $h^2 =$ mean-square sea wave height
  $\phi(x) =$ error function of argument x

Two constants t_p and t_s appear in this model.
In normal satellite operation, t_s will be much
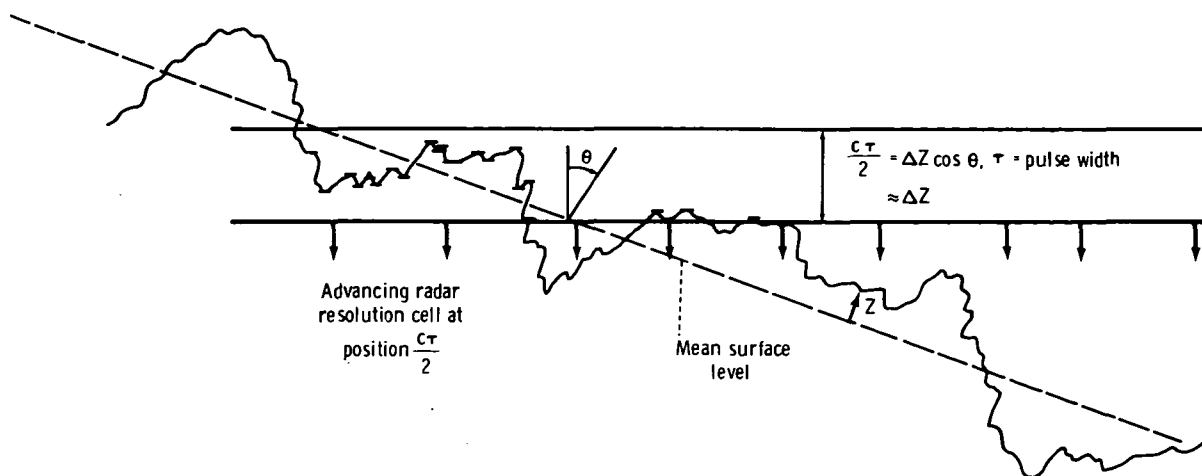larger than t_p; this is defined as the "pulse

FIGURE 3-13.—Physical illustration of specular point scatter (specular points are highlighted).

limited" mode of altimeter operation. In this case, the return signal (as expressed by the average radar cross section as a function of time in eq. (3–12)) is as shown in figure 3–15. The slope of the leading edge of the signal is a function of the significant sea-wave heights $H_{1/3}$ at the suborbital point. This portion of the signal is the one that must be used to extract "sea state."

The constants t_p and t_s have simple geometric interpretations that help to explain the nature of the received signal. As shown in figure 3–16, t_p represents the amount that the incident signal (propagating vertically downward) gets stretched by ocean waves of height h. The constant t_s is a measure of the time that the radar echo is being received from the sea, as shown in figure 3–14. In the pulse-limited mode $(t_s \gg t_p)$, this return will be received from a spherically advancing resolution cell as long as (1) there are specular points with slopes large enough to backscatter, and (2) the antenna beamwidth is great enough to permit illumination of the sea. For pulse-limited operation, the length of the trailing edge of the pulse shown in figure 3–15 is essentially t_s.

Because the information on significant sea-wave height for pulse-limited altimeter operation is contained in the slope of the leading edge, one way of retrieving the height distribution information is to differentiate (as a function of time) the averaged leading edge. This derivative is then essentially a pulse that is directly proportional to the ocean-wave height probability density function. This effect is shown in figure 3–17, in which a more realistic height distribution than the symmetric Gaussian function is now used. Oceanographers have known that, for greater wave heights, the height probability
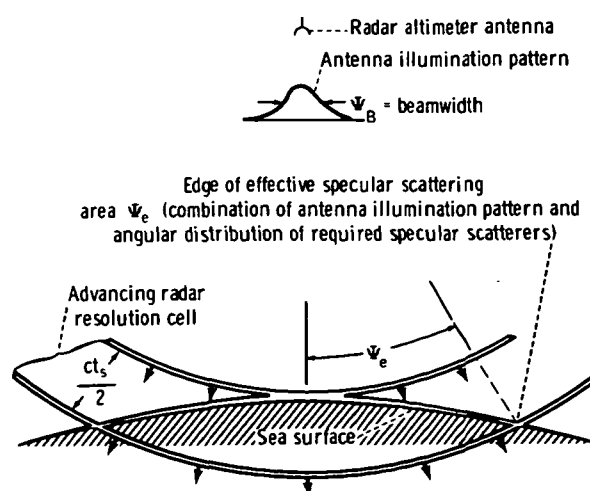

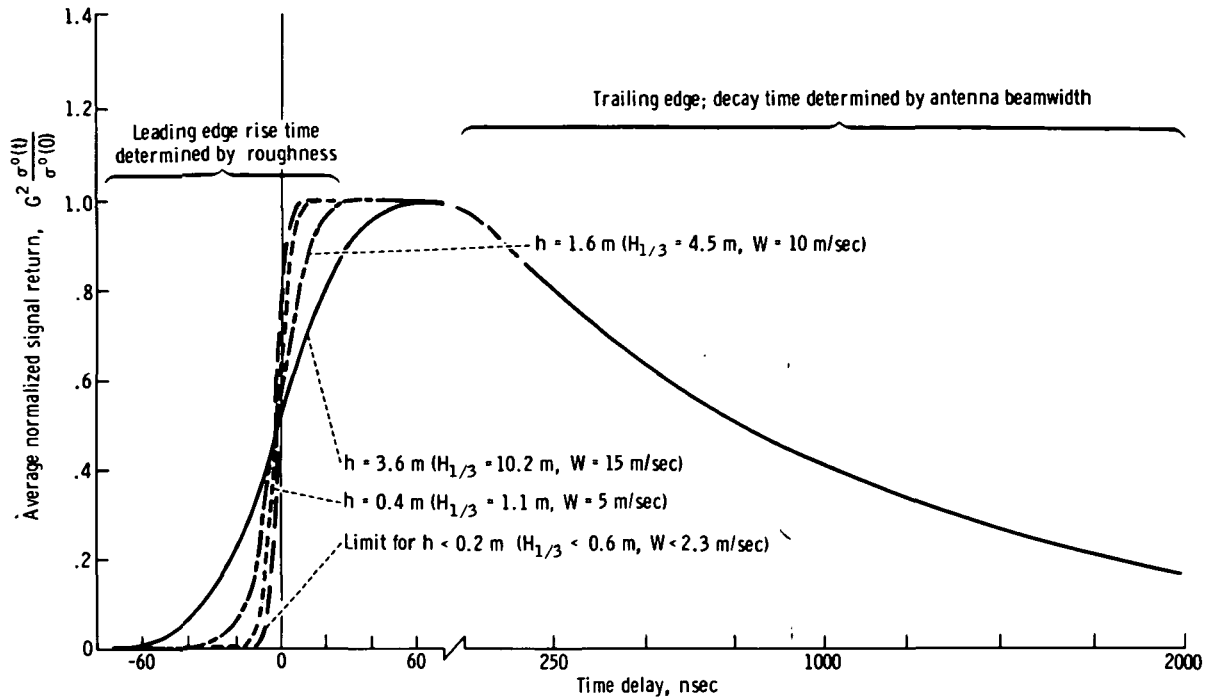FIGURE 3-14.—Interpretation of altimeter model constant t_s.

FIGURE 3–15.—Average radar cross section as a function of time (where $H_{1/3}$ is significant wave height and W is windspeed).

density function is skewed toward heights above the mean plane. This skewness can be described by a parameter δ, which can be as high as 0.4. Hence, the upper graphs in figure 3–17 show wave probability density functions (with and without skewness) for various wave heights. The lower graphs show the time derivative of the averaged leading edge of the received signal for a 10-nsec transmitted pulse (in the absence of noise). This signal, for greater wave heights, is stretched in direct proportion to the width of the height probability density function. However, note that when the height density function is skewed (dashed curve), the radar return is also skewed, but in the opposite direction. This has been observed experimentally, where the radar "centroid" of the measured altimetry return appears to move toward the troughs and away from the wave crests. The theoretical model explains this shift and can be used as a correction to quantitatively determine the error factor introduced by wave skewness for the purpose of determining the mean sea position.

The specular-point model, and its extension to radar altimetry, therefore adequately explains the interaction mechanism with the sea and can permit both the design of the sensor and the interpretation/extraction of sea-wave height information from the received signal.
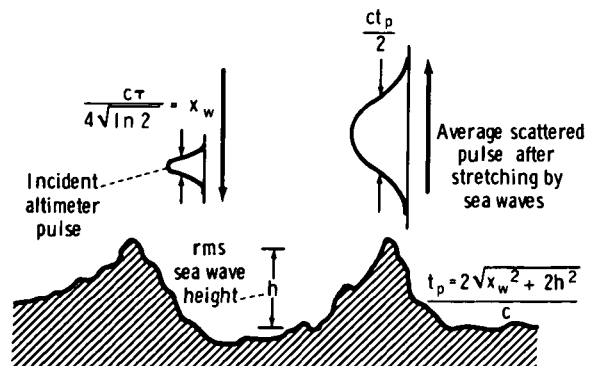

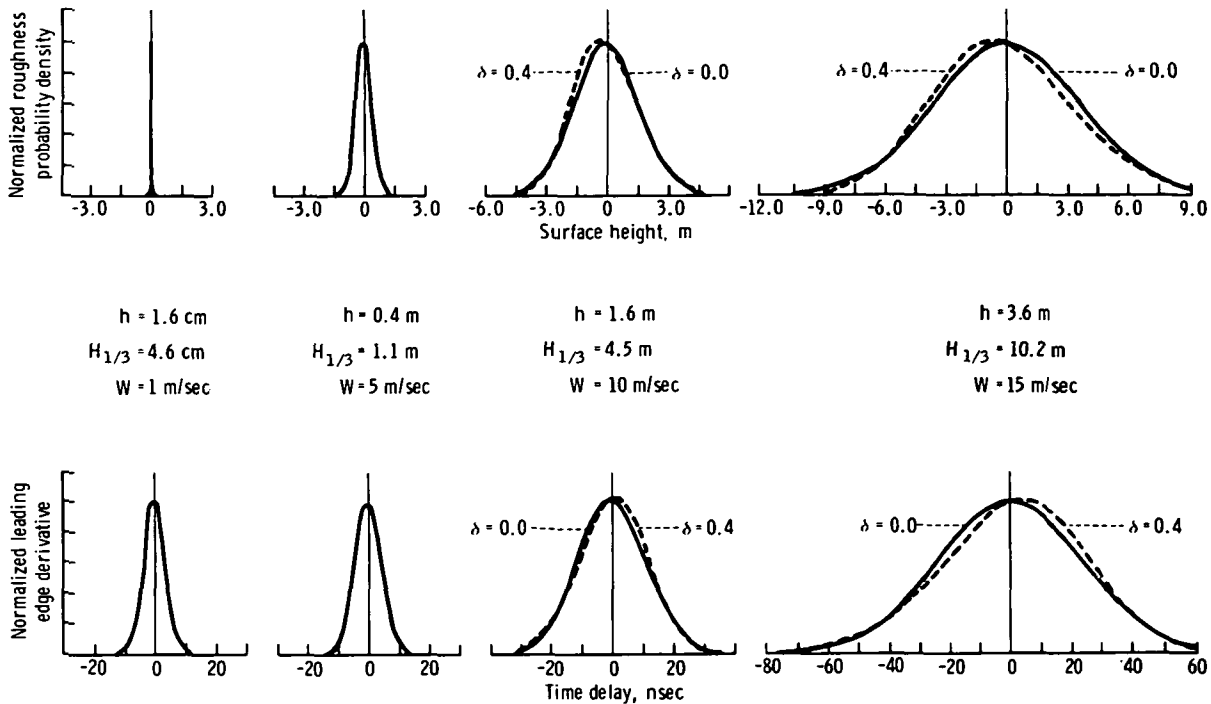FIGURE 3–16.—Interpretation of altimeter model constant t_p.

FIGURE 3–17.—Wave probability density functions.

Imaging Radars

Recently, airborne imaging radars have recorded very striking radar "pictures" of longer ocean-wave patterns that very clearly show the periods and directions of the various "swell type" wave components present on the sea. These high-resolution radar images are formed by synthetic aperture techniques, in which fine detail parallel to the flightpath is obtained by "synthesizing" a long antenna from the small aircraft antenna by combining the received signals at different points along the aircraft flightpath.

The purpose of this section is to explain that factor in the scatter process that permits the imaging radar to see the long gravity waves. For this purpose, it is adequate to consider only a high-resolution radar with a resolution cell size that is small in terms of the ocean wavelengths under observation, and to ignore the mechanical details of how the signal is processed aboard the aircraft to actually achieve this image. Because the imaging radar appears to have such great long-term potential for oceanic sensing from spacecraft, this understanding of the scatter process appears to be essential to the proper interpretation of the images in terms of sea state (or the wave-height directional spectrum).

The fact that the imaging radar "sees" gravity waves tens of meters in length (when the radar wavelength itself is only centimeters) indicates that the long wave is "modulating" the intensity of the echo over different parts of the wave. The most distinctive wave patterns in these radar images appear within approximately 25° from the vertical. The specular-point theory explains scatter in this region (see the section entitled "Physical Mechanisms of the Radar Echo"). Because the specular points producing scatter at centimetric radar wavelengths are themselves ocean-wave features with dimensions that are centimetric in scale, these small-wave features obviously must be affected by the presence of the long wave on which they are riding.

There are mechanisms by which modulation of the small specular-point scatterers can be produced by a long underlying gravity wave, thus enhancing the radar visibility of the long gravity wave. If one assumes (to first order) that the total slope of the surface is the sum of the slopes of all the surface components present, then the long gravity wave causes all the surface components present and also causes all the small-wave specular points to be tilted according to its own slope. Thus, for the radar look direction shown, more specular points will be on the forward face of the wave than on the back side. The diagram in figure 3–18 illustrates this modulation pattern as a "radar reflectivity plot," in which the heavier shading corresponds to the greater reflectivity on the forward wave face. Hence, a periodic pattern of radar reflectivity is produced that corresponds to the long underlying gravity wave. The equations under the plot use the previous specular-point model (eq. (3–2)) to show how the slope probability density function of the small wavelets is modified to account for the presence of the long wave slope ζ_x^ℓ. The
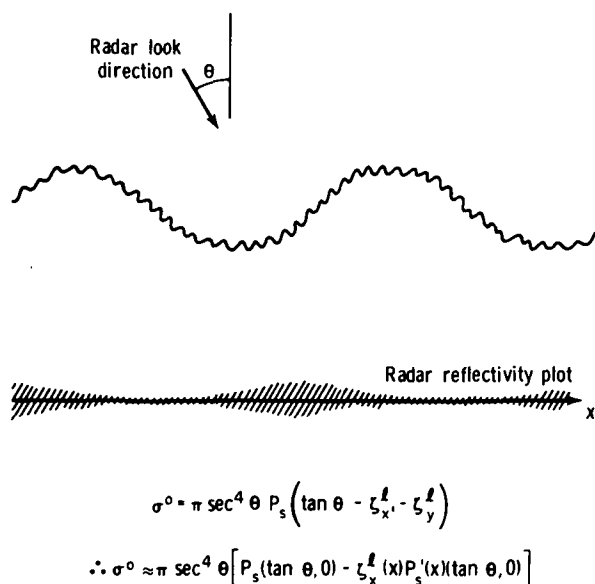
second equation expands the small-scale slope density function in a Taylor series, showing that (to first order) the radar cross section is indeed proportional to the slope of the long underlying gravity wave. This explains why the longer wave is visible and also provides a quantitative estimate of the intensity of this modulation.

A second mechanism (fig. 3–19) can also produce a radar reflectivity pattern that carries the modulation of a long underlying gravity wave. As a result of hydrodynamic nonlinear interactions involving straining and surface tension, short capillary waves tend to be concentrated more on the leading edge of the long gravity wave. The leading edge is defined as the side of the long wave the normal of which points in the same direction as its phase velocity. Capillary waves are excited by very gusty, strong winds and hence may be absent entirely when there is little wind. When they are present, however, they will arrange themselves in a spatial pattern with the periodicity of the underlying gravity wave and thereby produce a radar cross section that (to first order) varies directly with the slope of the underlying gravity wave. The proportionality constants, which depend on wind, are presently unknown. They could be estimated either theoretically or experimentally.

One final effect may (in some cases) account for the "wave" patterns seen by an imaging radar. This effect is the orbital velocity of the short radar-reflecting capillary waves due to the presence and motion of the long underlying gravity wave. These scat-
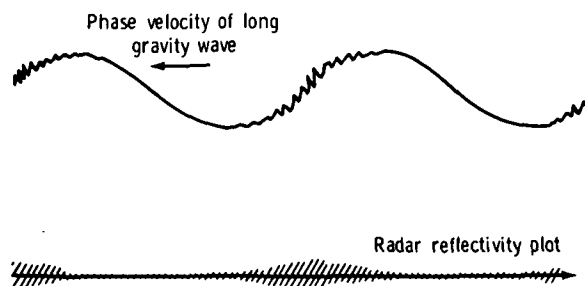

$$\sigma^0 = \pi \sec^4\theta \; P_s\left(\tan\theta - \zeta_{x'}^\ell - \zeta_y^\ell\right)$$

$$\therefore \sigma^0 \approx \pi \sec^4\theta\left[P_s(\tan\theta, 0) - \zeta_x^\ell (x)P_s'(x)(\tan\theta, 0)\right]$$

FIGURE 3–18.—Specular-point tilt superposition (where P_s is the probability density function in the specular direction).

FIGURE 3–19.—Capillary bunching on leading edge.

tering specular points on the larger gravity wave execute a circular motion as the longer wave passes beneath them. For a given position of the long wave, the direction of this circular motion is in the directions shown by the arrows in figure 3–20. The speed v_0 of this motion is constant and equals $2a[(2\pi g)/L]^{1/2}$, depending on the amplitude a and length L of the long wave. Therefore, at some points on the long wave, the specular points have no component of motion along the radar direction (where the vector is perpendicular to the radar line of sight). At other points (in particular, within two regions over one period of the longer wave), the orbital velocity component lies along the radar look direction, and the specular points are moving relative to the radar and hence changing their phase with time, as observed at the radar receiver. Because the return from the sea in an imaging radar is observed and integrated for some finite period of time T, the distance traveled by these "maximum radial velocity" specular regions during this time is v_0T. If this distance is greater than one-quarter of the radar wavelength, destructive phase interference will occur in these regions and the "image" will appear weaker (or effectively "blurred"). For example, for a long wave with an amplitude of 1 m and a length of 15 m, destructive interference will occur for processing times greater than 6

msec when viewed at S-band frequencies (10 cm).

The radar reflectivity plot corresponding to this temporal smearing effect is shown in figure 3–20. The important fact is that this effect, unlike the previous two, produces a reflectivity plot that appears as a second spatial harmonic of the fundamental gravity wave. Thus, the radar image would give the misleading impression that the ocean wave seen by the radar was one-half its actual length.

Which of the three mechanisms is dominant is not clear. Because only the first has been analyzed quantitatively, the others, at this time, can only be qualitatively described and said to have some part in the production of the radar image. Further analysis is required on the latter two to ascertain their quantitative role in the process. As can be seen from the reflectivity plots and from the equations, the three effects do not always reinforce each other constructively for all angles. Because, in addition, the specularly reflecting capillary waves are present on top of the long swell-type gravity waves only in gusty wind conditions, there may be several situations that involve combinations of effects in which the long gravity waves are not visible at all on radar images. This may explain the "sometimes" nature of swell patterns in radar images when compared to optical photographs.

MICROWAVE RADIOMETRY APPLICATIONS

The rationale of including a discussion on microwave radiometer measurements of the ocean surface is that some oceanographic parameters can best be made with radiometers (rather than radars). As noted in a previous section, using a radar to accurately measure ocean-surface temperature and salinity is unrealistic. Microwave radiometers, however, offer a very attractive possibility. A plot of brightness temperature as a function of salinity content of the water is shown in figure 3–21 for 1.0 and 5.4 GHz. Brightness temperature as a function of
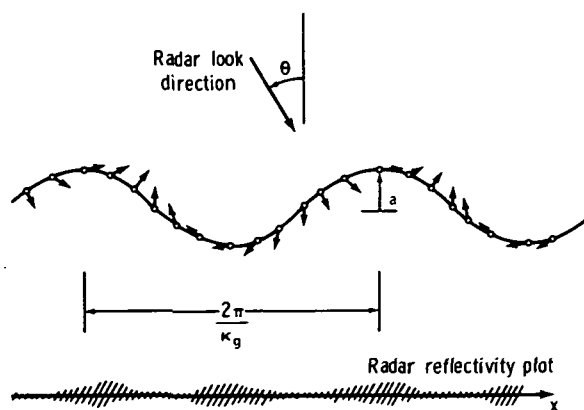

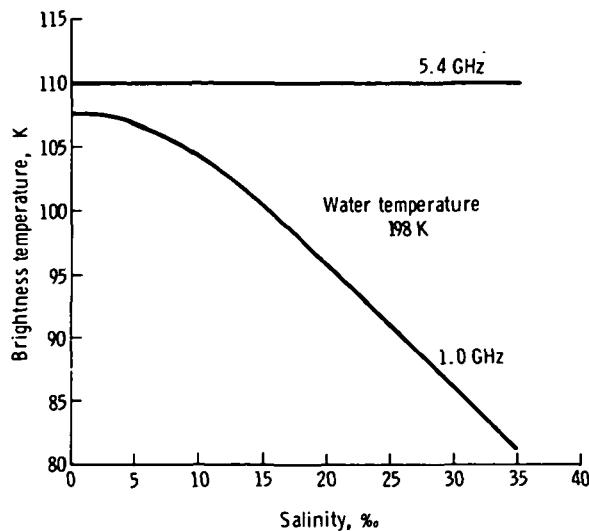FIGURE 3–20.—Capillary motion caused by orbital velocity.

FIGURE 3-21.—Brightness temperature as a function of salinity content.

water temperature is plotted for the same two frequencies in figure 3-22.

The relative independence of brightness temperature with salinity at C-band coupled with the strong salinity dependence at L-band suggests that an airborne two-frequency radiometer system can be used to measure water temperature and salinity. An S-band radiometer developed for the NASA AAFE has demonstrated the capability of measuring brightness temperature to an accuracy of 0.3 K. A companion instrument operating at L-band (which is being constructed at LaRC) would open the possibility of simultaneously measuring water temperature and salinity to respective accuracies of at least 1 K and 1‰. The 1‰ accuracy figure for the salinity measurement is valid only if the salinity is greater than 5‰.

The most attractive use of the microwave radiometer is as an instrument to complement the scatterometer for wind measurements. Radiometers may be required to provide atmospheric corrections for active measurements.

CONCLUSIONS AND RECOMMENDATIONS

There is firm experimental evidence to conclude that the electromagnetic backscattering process at microwave frequencies is due to (1) specular-point reflections when the viewing angle is within 20° of nadir, and (2) resonant (Bragg) scattering when the viewing angle is beyond 20° from nadir. The first phenomenon is intimately linked to the tilt of gravity waves, and the second is due to the spectral characteristics of the capillary or short gravity wave spectrum.

The response of the radar altimeter can be interpreted in terms of the specular-point theory; that is, the impulse response is stretched in time in a manner that is proportional to the vertical distribution of specular points.

The scatterometer measures sea slope near vertical incidence as a result of the change in the rms tilt of specular points. At angles sufficiently removed from the vertical, the scatterometer responds to the wind fields because of the instantaneous change in the Bragg spectrum of short waves.

More analytical work is required to define the scattering process associated with promising experimental techniques, including the imaging radar. Microwave radiometers
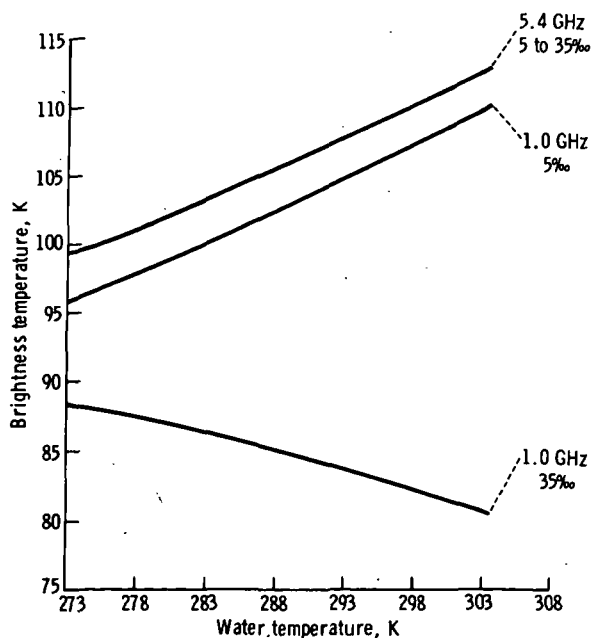

FIGURE 3-22.—Brightness temperature as a function of water temperature.

should be incorporated as complementary instruments, specifically in regard to ocean temperature measurements, salinity measurements, and inference of high windspeeds due to the presence of surface foam.

Parallel analytical and experimental efforts are recommended to establish the accuracy with which windspeed can be measured from the percent foam coverage.

PART C

LOCAL PHENOMENA

This section is devoted to the oceanic and coastal phenomena with dimensions ranging to 100 km. The two major categories discussed are waves (their generation and dynamics) and ocean-land related problems.

The dynamics of surface waves in both capillary and gravity ranges indicates that microwave technology provides a superior means of measuring simultaneously the spatial and temporal properties of ocean waves. The need for basic studies of physical phenomena in support of active microwave sensing is indicated. Active microwave scattering from surface waves is discussed in terms of wave dynamics. Ocean waves receive most of their energy from wind. The state of the art in wind measurements by conventional methods shows a gross inadequacy of present surface-sampling techniques for global weather and wave forecasting; microwave technology offers the potential to alleviate many of the problems. Global aspects of wind climatology are included in the discussion of large-scale phenomena in the section entitled "Global Wave Statistics." The subject of internal waves is relatively new and is less well understood in comparison with surface waves. Internal waves, even though they exist well below the microwave skin depth, are frequently detectable through surface manifestations such as convergence zone slicks, which have been visible in Earth Resources Technology Satellite (ERTS) imagery. Internal waves may also possibly be detected from surface temperature anomalies in the divergence zones. Thus, by

monitoring surface properties with microwave sensors, a mathematical model for the prediction of internal waves might be developed.

The second category deals with the interaction between the ocean and its land boundaries in the coastal zone. The monitoring of shoreline changes is very important for coastal engineering and oil-drilling structures, beach erosion, coastal navigation, and recreation. The wave climate, the single most important parameter affecting coastal processes, could be monitored in great detail over large areas by satellite-borne active microwave sensors.

All these phenomena influence the ocean-surface structure in various ways, which are detectable by active microwave instruments. The signatures of signals obtained by such instruments and their relationships to oceanic and coastal processes provide an invaluable aid to understanding these processes.

WAVES

Human activities on the sea are very much influenced by waves, which damage structures and cargoes, change shorelines, and slow the progress of ships. A better understanding of waves and better wave predictions will benefit marine activities and yield concomitant economic benefits.

In the past, wave measurements have been difficult, and understanding of the generation, propagation, mutual interaction, and decay of waves on the ocean is based on several good oceanographic experiments. In